

Article

# Method Combining Probability Integration Model and a Small Baseline Subset for Time Series Monitoring of Mining Subsidence

Hongdong Fan <sup>1,\*</sup>, Lu Lu <sup>2,\*</sup>  and Yahui Yao <sup>3</sup>

<sup>1</sup> Key Laboratory for Land Environment and Disaster Monitoring of NASG, China University of Mining and Technology, Xuzhou 221116, China

<sup>2</sup> School of Environment Science and Spatial Informatics, China University of Mining and Technology, Xuzhou 221116, China

<sup>3</sup> Center for Hydrogeology and Environmental Geology Survey, CGS, Baoding 071051, China; yahui4869@126.com

\* Correspondence: ywfhdcumt.edu.cn (H.F.); cumtlulu@cumt.edu.cn (L.L.); Tel.: +86-158-6216-5361 (H.F.); +86-177-5198-3782 (L.L.)

Received: 30 July 2018; Accepted: 6 September 2018; Published: 10 September 2018



**Abstract:** Time Series Interferometric Synthetic Aperture Radar (TS-InSAR) has high accuracy for monitoring slow surface subsidence. However, in the case of a large-scale mining subsidence areas, the monitoring capabilities of TS-InSAR are poor, owing to temporal and spatial decorrelation. To monitor mining subsidence effectively, a method known as Probability Integration Model Small Baseline Set (PIM-SBAS) was applied. In this method, mining subsidence with a large deformation gradient was simulated by a PIM. After simulated deformation was transformed into a wrapped phase, the residual wrapped phase was obtained by subtracting the simulated wrapped phase from the actual wrapped phase. SBAS was used to calculate the residual subsidence. Finally, the mining subsidence was determined by adding the simulated deformation to the residual subsidence. The time series subsidence of the Nantun mining area was derived from 10 TerraSAR-X (TSX) images for the period 25 December 2011 to 2 April 2012. The Zouji highway above the 9308 workface was the target for study. The calculated maximum mining subsidence was 860 mm. The maximum subsidence for the Zouji highway was about 145 mm. Compared with the SBAS method, PIM-SBAS alleviates the difficulty of phase unwrapping, and may be used to monitor large-scale mining subsidence.

**Keywords:** probability integration model; SBAS; mining subsidence; deformation monitoring

## 1. Introduction

China is a country whose main energy source is coal; coal resources account for more than 70% of China's energy structure, and this pattern is expected to continue into the future. Goafs are formed after underground coal mining. The upper rock layers of goafs undergo deformation, bending, movement, and collapse under gravity, and the rock deformation spreads to the surface and results in surface subsidence basins. About 14 billion tons of coal are compressed under buildings, railways, and water-bodies in China; the extraction of these coal seams has theoretical and practical significance for the economic recovery of the coal resources and protection of ground structures [1].

To monitor mining subsidence, geodetic technologies, which comprise total station surveying, precise leveling measurement, global navigation satellite system (GNSS), and GPS networks, have been used widely. These traditional methods suffer some limitations due to the need for long observation periods. Additionally, these methods are labor-intensive and costly. As a new earth observation technology, differential interferometry synthetic aperture RADAR (DInSAR) has many

advantages, such as immunity to weather conditions, large-scale coverage, high spatial resolution, and repeated observation. Thus, DInSAR has been used in volcanic activity monitoring [2,3], landslip monitoring [4], and seismic activity monitoring [5]. In particular, DInSAR has been used to monitor surface deformation in mining areas. In particular, DInSAR has a high monitoring precision for residual surface subsidence caused by abandoned goafs. However, rapid deformations and sudden collapses in mining areas are difficult to monitor effectively with conventional DInSAR.

Since the Persistent Scatterer InSAR (PS-InSAR) [6] was proposed in 2001, time series InSAR has been rapidly developed and widely used. There are, however, two disadvantages to PS-InSAR: (1) Permanent scatterers, which maintain a high coherence over the study period, are needed; (2) a large number of images (20–30) are required for statistical analysis, which limits application in non-urban areas. The use of the small baseline set (SBAS) was proposed by Berardino et al. [7]. However, in this case, the resolution of images is reduced when coherent points are selected, and the interferograms are required to be unwrapped. PS-InSAR and SBAS minimize the limitations of traditional InSAR, which include atmospheric errors, orbit errors and terrain errors [8–11]. Referring to PS-InSAR and SBAS, numerous time series InSAR technologies have been proposed, such as StaMPS (Stanford Method for Persistent Scatterers) [12], TCPInSAR (Temporarily Coherent Point InSAR) [13,14], IPTA [15], CPT [16], and so on. To improve the number of coherent points in non-urban areas, the use of distributed scatterers (DS) [17] was proposed by Rocca et al. Further, SqueeSAR [18], which combines permanent scatterers and distributed scatterers, was reported by Ferretti et al. Recently, researchers have studied the use of CAESAR (Component extrAction and sElection SAR) [19] and PD-PSInSAR (phase decomposition based PS-InSAR) [20]. Phase decomposition, variance matrix decomposition, and other methods are used to analyze the scattering mechanisms underlying spatial and temporal decoherence, and to obtain more permanent and distributed scatterers.

Surface subsidence caused by coal mining takes place over a significant timescale. The subsidence may last for several years or even decades. Therefore, time series InSAR technologies are used to obtain time series surface subsidence information in order to study the subsidence mechanism, land reclamation, and foundation stability. Accordingly, numerous researchers have applied time series InSAR to monitor subsidence in abandoned goaf areas [21,22]. Because of differences in energy structure, the exploitation of coal mines has gradually declined in North America, Europe and other regions. Time series InSAR technologies have been used to monitor the surface deformations due to coal mining in Germany [23], England [24], and other regions. For example, PSI was used by Cuenca et al. [23] to study the relationship between the groundwater level of abandoned mines at the junction of the Netherlands, Belgium, and Germany, and to determine the surface deformation. The monitoring results indicated that the maximum deformation was most elevated (up to +220 mm) from 1992 to 2009. Intermittent SBAS-InSAR (ISBAS) [24] was proposed by Bateson et al. and used to monitor the surface deformation of the South Wales coalfield from 1992 to 1999.

Coal resources continue to represent a large proportion of China's energy structure, and deposits are widely distributed in central, western, and northwestern China. Many coal mines have been exploited, and there is a large incidence of surface subsidence. Time series InSAR has been used to monitor surface subsidence in coalfields such as Huaibei [25], Yanzhou [26], Yulin [27], and Fengfeng [28]. A method that combines DInSAR and probability integration was introduced by Fan et al. [25] to monitor large-magnitude deformation in the Huaibei coalfield. Using DInSAR combined with Kalman filtering, the deformation of a highway in the Nantun coalfield region was analyzed by Zhao et al. [26]. TCPInSAR was used by Fan et al. [27] to monitor surface deformation in the Yulin mining area from October 2012 to March 2013. The results indicated that the maximum deformation reached  $-86$  mm.

The application of time series InSAR for subsidence monitoring in mining areas remains limited by several challenges: (1) Surface subsidence caused by coal mining reveals unique characteristics, such as non-linearity, sudden collapse and huge subsidence, which results in erroneous phase unwrapping. Errors are introduced during the processing of the SBAS. (2) Coal mines are generally located

below farmland; as a result, high-coherence point targets are scarce, as the land surface is covered by vegetation.

## 2. Study Area and Datasets

The study area is the 9308 workface in the Nantun mining area (Jining City, Shandong Province, China), where the land surface consists mainly of industrial plants and farmland. The Zouji highway also passes over the workface. The strike length and dip width of this workface are 800 m and 140 m, respectively. The average mining depth is about 630 m. The thickness of the coal seam is about 4.76 m. The coal seam has an inclination angle of  $6^\circ$ , and the mining direction was from the northeast to southwest. The 9306 workface, located on the southeast side of the 9308 workface, is an abandoned goaf, where work ceased in 2011. The location of the 9308 and 9306 workfaces are shown in Figure 1. The purple frame represents the scope of mining during the study period, and the black arrow represents the direction of coal mining. To effectively monitor the subsidence that occurred on the Zouji highway, a total of 21 ground leveling points, whose layouts were from east to west along the highway, were selected to monitor the subsidence. These ground leveling points are annotated using red dots and labeled using white characters.

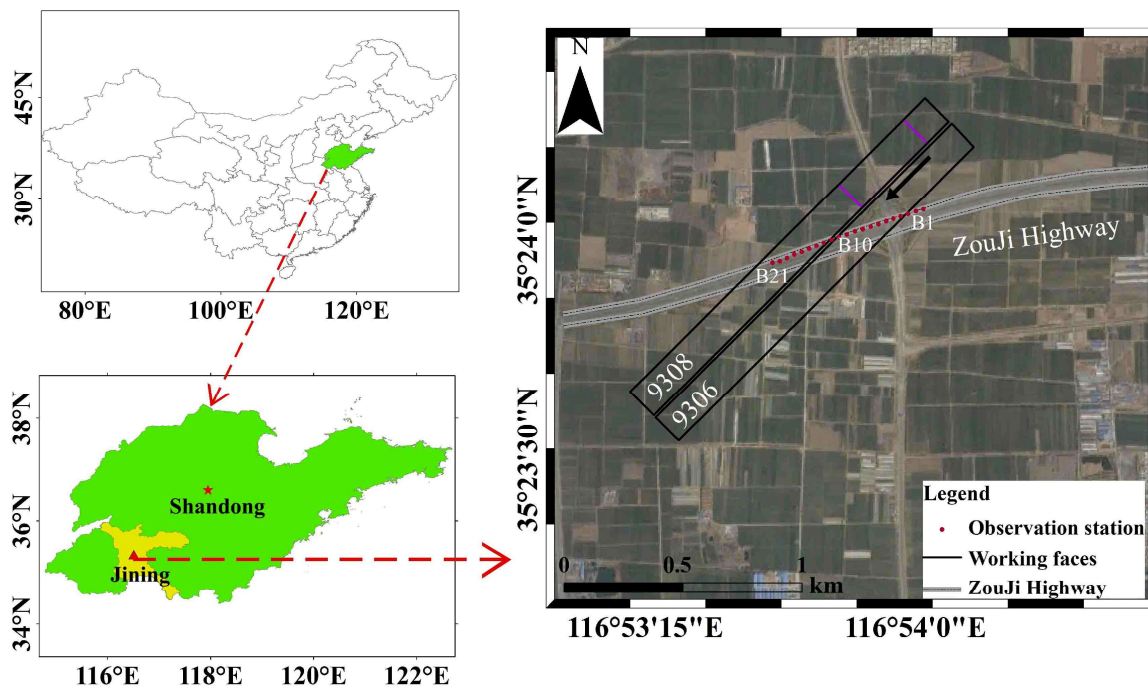


**Figure 1.** Location of the study area in Jining, Shandong Province, east China. The two black frames are the 9306 and 9308 workfaces, respectively. The purple frame represents the extent of mining from 25 December 2011 to 2 April 2012.

The main impacts from coal mining on the surface are ground fissures and subsidence. The exploitation of these coal seams, which are located under buildings, railways, and highways, affects the safety, stability, and integrity of these structures. To safeguard human life, property, and the road infrastructure, there is an urgent need to monitor the subsidence caused by coal mining. The monitoring results should provide a basis for highway maintenance and management.

In this study, ten TerraSAR-X images, spanning the period from 25 December 2011 to 2 April 2012, were acquired. The TerraSAR-X satellite (TSX), launched by the German Aerospace Center (DLR) on 15 June 2007, is synchronized to the sun. Compared with other SAR satellites, the repetitive observation period of the TSX is 11 days, which enables an increase in the frequency of subsidence monitoring. The range and azimuth of pixel spacing are about 1.5 m and 2.0 m, respectively. To preserve a high

coherence for all image pairs, only image pairs with the smallest temporal and spatial baseline were selected. A total of nine image pairs, which were constructed from two adjacent images, were generated. The specific parameters of the nine image pairs are shown Table 1.

**Table 1.** Parameters of TSX images pairs.

Master Image	Slave Image	Spatial Baseline/m	Temporal Baseline/day
25 Dec. 2011	5 Jan. 2012	−25.1171	11
5 Jan. 2012	16 Jan. 2012	104.0496	11
16 Jan. 2012	27 Jan. 2012	7.2308	11
27 Jan. 2012	7 Feb. 2012	90.6461	11
7 Feb. 2012	18 Feb. 2012	−140.2636	11
18 Feb. 2012	29 Feb. 2012	143.7575	11
29 Feb. 2012	11 Mar. 2012	−162.4879	11
11 Mar. 2012	22 Mar. 2012	136.6069	11
22 Mar. 2012	2 Apr. 2012	−90.9748	11

### 3. Methodology

#### 3.1. Probability Integration Model

During the deposition process, different rock formations are formed due to changes in the sedimentary environment, and layers appear at the interface of different rock strata. However, the rock strata are affected by late tectonic stress and magma intrusion, and weak surfaces such as joints, bedding, and faults are formed in the rock stratum. Due to the existence of weak surfaces, probability integration model, which is widely used for subsidence prediction with coal mining, idealizes the formation as a discontinuous loose medium, and the formation deforms as the coal is mined [1].

The PIM was constructed in the 1960s using random media theory proposed by Polish scholars. The PIM regards the strata movement as a stochastic process that obeys statistical laws, and the probability density function integral formula is used to predict surface subsidence caused by coal mining. The basic idea is to treat the movement of surface and rock as a random event, whereby the mining area is represented as an infinite number of tiny units, and then to calculate the sum of influences of all the units on rock formation and surface deformation. This approach is the most widely used method for subsidence prediction in China [1,29].

As shown in Figure 2, the ground coordinate system  $xOy$  and the coal seam coordinate system  $uO1v$  are assembled. The unit  $B(u, v)$  is seen as a unit in the inclined coal seam. According to the PIM, unit extraction will cause movements of point  $A(x, y)$  on the surface. The value can be expressed as:

$$W_e(x, y) = \frac{1}{r^2} \exp\left(-\pi \frac{(x-u)^2 + (y-v + Hc \tan \theta)^2}{r^2}\right) \quad (1)$$

where  $r$  is the main influence radius of unit  $B$  and  $r = H / \tan \beta$ ,  $H$  is the depth of unit  $B$ ,  $\tan \beta$  is the main influence angle tangent, and  $\theta$  is the mining influence propagation angle.

Formula (1) represents the surface movement caused by a mining unit. If the entire coal seam is extracted, according to the principle of superposition, the movement  $W(x, y)$  of point  $A(x, y)$  on the surface caused by mining is given by expression (2):

$$W(x, y) = W_0 \int_{s_3}^l \int_{s_1 \cos \alpha}^L W_e(x, y) dv du \quad (2)$$

where  $W_0$  is the maximum subsidence for this geological condition of the mine,  $W_0 = mq \cos \alpha$ ,  $m$  is the coal seam thickness,  $q$  is the subsidence coefficient,  $\alpha$  is the dip angle of the coal seam,  $l = D_3 - s_4$ ,  $L = (D_1 - s_2) \cos \alpha$ ;  $D_1$  and  $D_3$  are the strike length and inclined length of the work face, respectively;

$s_1$ ,  $s_2$ ,  $s_3$  and  $s_4$  are the displacement distances of the inflection point in the downhill, uphill, left, and right directions of the workface, respectively.

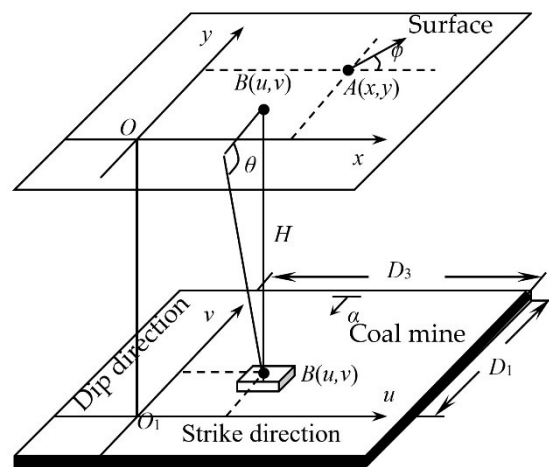


**Figure 2.** Geometric relationship between underground coal mining and the surface target.

Therefore, using the geological mining data, the dynamic surface subsidence caused by coal extraction can be simulated by the PIM; the precision of estimation is mainly related to several basic parameters, including the subsidence coefficient ( $q$ ),  $\tan \beta$ ,  $\theta$ , the coal seam thickness, and the mining depth.

### 3.2. SBAS

SBAS, which was proposed in 2002, has overcome the limitations of PS-InSAR, and has been widely applied in various fields of deformation monitoring. SAR images are combined into interference pairs via the restriction of small spatial and temporal baselines. Points with high coherence are selected, and terrain phases are removed by the external digital elevation model (DEM) to obtain differential interference phases. A functional relationship is established between the unwrapped differential interferometric phase and the surface deformation rate, and  $v$  and  $\epsilon$  are calculated using the least squares method or by the singular value decomposition method. This approach has many advantages, including simple principles for estimation and easy implementation, and is not limited by the quantity of images. Further, the selection of high coherence points reduces the image resolution. In areas with larger magnitude deformation and large vegetation coverage, errors are readily introduced into the phase unwrapping process because of decorrelations.

We assume that the number of differential interferograms is  $I$ , the differential interferometric phase  $\Delta\phi_i$  of the  $i$ th interferogram can be expressed as Formula (3).

$$\Delta\phi_i = -\frac{4\pi B_{\perp}}{\lambda r \sin(\theta)} \epsilon + \frac{4\pi}{\lambda} T_i v_i \tag{3}$$

where,  $\lambda$  is wavelength,  $r$  is the distance in the LOS direction,  $\theta$  is the angle of incidence,  $B_{\perp}$  is the vertical baseline,  $\epsilon$  is the terrain error, and  $T_i$  and  $v_i$  are the temporal baseline and the velocity of deformation of the  $i$ th interference pair, respectively.

We assume that

$$kz_i = -\frac{4\pi B_{\perp}}{\lambda r \sin(\theta)} \tag{4}$$

$$kt_i = \frac{4\pi}{\lambda} T_i \tag{5}$$

Formula (3) can be expressed as Formula (6).

$$\begin{bmatrix} kt_1 & 0 & 0 & \cdots & kz_1 \\ 0 & kt_2 & 0 & \cdots & kz_2 \\ \cdots & \cdots & \cdots & \cdots & \cdots \\ 0 & 0 & 0 & kt_I & kz_I \end{bmatrix} \begin{bmatrix} v_1 \\ \cdots \\ v_I \\ \varepsilon \end{bmatrix} = \begin{bmatrix} \Delta\phi_1 \\ \Delta\phi_2 \\ \cdots \\ \Delta\phi_I \end{bmatrix} \quad (6)$$

where  $I$  is the number of interference pairs.

Assuming that subsidence is linear with time, relationship between subsidence and time can be expressed as Formula (7).

$$v_i = \frac{x_{si} - x_{mi}}{T_i} \quad (7)$$

where  $x_{si}$  ( $si = 2, 3 \dots N$ ,  $N$  is the number of SAR images),  $x_{mi}$  ( $mi = 1, 2 \dots N-1$ ) are the accumulated subsidence of coherent point on  $i$ th differential interferogram fore slave image and master image respectively, and  $T_i$  is the temporal baseline of the  $i$ th interference pair. Time-series subsidence of coherent points is accumulated using Formula (8).

$$\begin{bmatrix} -1 & 1 & 0 & \cdots & 0 \\ -1 & 0 & 1 & \cdots & 0 \\ \cdots & \cdots & \cdots & \cdots & \cdots \\ 0 & 0 & -1 & \cdots & 1 \end{bmatrix} \begin{bmatrix} x_1 \\ x_2 \\ \cdots \\ x_N \end{bmatrix} = \begin{bmatrix} v_1 T_1 \\ v_2 T_2 \\ \cdots \\ v_I T_I \end{bmatrix} \quad (8)$$

### 3.3. PIM-SBAS

A new methodology, which combines the PIM and SBAS, is proposed in this study. To avoid the errors introduced by temporal and spatial decorrelations into the phase unwrapping step, mining subsidence could be effectively simulated using PIM-SBAS. The specific steps are as follows (Figure 3): (1) DInSAR is used to yield the actual wrapped phase; (2) the time series surface deformations are simulated using PIM and the geological mining parameters; (3) the simulated surface subsidence is converted to wrapped phases, and the wrapped phases are subtracted from the actual wrapped phase to obtain the residual phase; (4) SBAS is used to determine the residual deformations; (5) the total surface deformation is determined by adding the residual deformation to the simulated surface deformation.

### 3.4. Validation Methods of the Results

#### 3.4.1. TCPInSAR

TCPInSAR, which was proposed by Zhang et al. [13,14] in 2011, has been used in calculating surface subsidence using temporarily coherent points (TCPs) rather than persistent coherent points. After identifying TCPs from images over the whole time span, the local Delaunay triangulation network is used to assist in connecting all the TCPs and each connected pair in the network is termed as an arc. In the model, the arcs with phase ambiguity are detected and removed using least squares residuals.

In the  $i$ th differential interferogram, the differential phase of the TCP with the coordinate  $(l, m)$  can be expressed as:

$$\phi_{l,m}^i = W \left\{ \phi_{topo,l,m}^i + \phi_{def,l,m}^i + \phi_{atmo,l,m}^i + \phi_{orbit,l,m}^i + \phi_{dop,l,m}^i + \phi_{noise,l,m}^i \right\} \quad (9)$$

where  $W\{ \}$  is the phase wrapping operation,  $\phi_{topo,l,m}^i$  is the topography phase error,  $\phi_{def,l,m}^i$  is the deformation phase,  $\phi_{atmo,l,m}^i$  represents the atmospheric artefacts,  $\phi_{orbit,l,m}^i$  is the orbit error phase,  $\phi_{dop,l,m}^i$  is the phase error of the difference of the Doppler phase and  $\phi_{noise,l,m}^i$  is the noise phase.

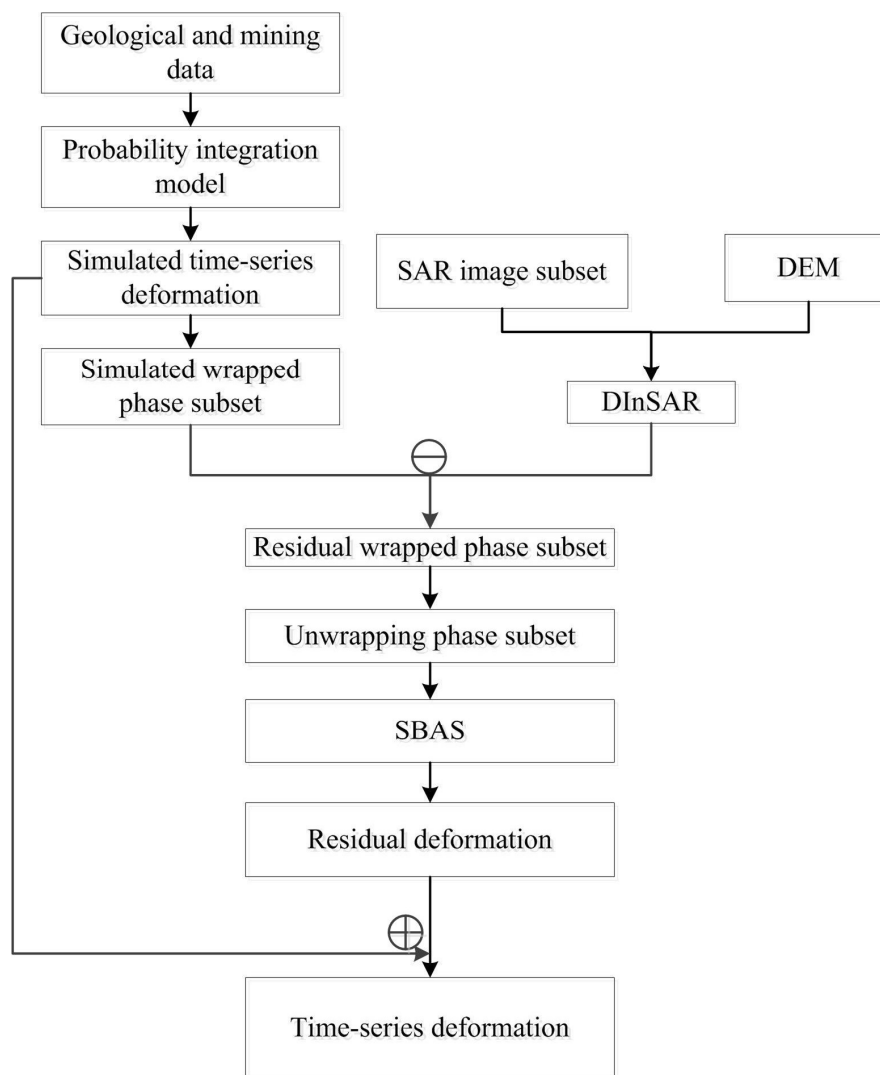


Figure 3. Flow chart for PIM-SBAS.

Land subsidence can be expressed by the deformation velocity and time intervals of SLC (single look complex) data. The topography phase error is related to the perpendicular baseline and altitude error  $\Delta h_{l,m}$ .

$$\phi_{def,l,m}^i = -\frac{4\pi}{\lambda} \sum_{k=1}^{C_i-1} (t_k - t_{k-1})v_k = \beta_i \mathbf{V} \quad (10)$$

$$\phi_{topo,l,m}^i = -\frac{4\pi}{\lambda} \frac{B_{perp,l,m}^i}{r_{l,m}^i \sin \theta_{l,m}^i} \Delta h_{l,m} = \alpha_{l,m}^i \Delta h_{l,m} \quad (11)$$

where  $C_i$  is the total number of SLC images between the acquired time of master and slave images,  $t_k$  is the acquired time of SLC images,  $\lambda$  is the wave length of the SAR,  $\mathbf{V}$  is the subsidence velocity vector,  $B_{perp,l,m}^i$  is the perpendicular baseline of the TCP point  $(l, m)$ ,  $\theta_{l,m}^i$  is the local incidence angle, and  $r_{l,m}^i$  is the slant range between the land target and the satellite.

The differential operation between a pair of nearby TCPs can reduce the atmospheric artefacts, the orbital error phase, so the phase difference of a given arc between two nearby TCPs can be written as:

$$\Delta \phi_{l,m,l',m'}^i = W \left\{ \alpha_{l,m,l',m'}^i \Delta h_{l,m,l',m'} + \beta_i \Delta \mathbf{V} + \omega_{l,m,l',m'}^i \right\} \quad (12)$$

where  $\omega_{l,m,l',m'}^i = \Delta\phi_{atmo,l,m,l',m'}^i + \Delta\phi_{orbit,l,m,l',m'}^i + \Delta\phi_{dop,l,m,l',m'}^i + \Delta\phi_{noise,l,m,l',m'}^i$ , which is the residual phases error vector and  $\Delta\mathbf{V} = [\Delta v_{l,m,l',m'}^1 \ \Delta v_{l,m,l',m'}^2 \ \cdots \ \Delta v_{l,m,l',m'}^I]^T$ .

When there are no phase ambiguities among all arcs in a Delaunay network, the phase difference of arcs can be simplified as:

$$\Delta\Phi = A \begin{bmatrix} \Delta h_{l,m,l',m'} \\ \Delta\mathbf{V} \end{bmatrix} + \mathbf{W} \tag{13}$$

where  $\Delta h_{l,m,l',m'}$  is the difference of height errors of an arc connected by two TCPs ( $l, m$ ), and ( $l', m'$ ),  $\Delta\mathbf{V}$  is the difference subsidence velocity between two TCP in an arc,  $\mathbf{W}$  is the residual phase error vector,  $A$  is the coefficient matrix. and  $\Delta\Phi$  is the phase difference between two TCPs in an arc.

The parameters  $\Delta\hat{V}$ ,  $\Delta\hat{h}$  and  $\hat{w}$  of the TCPs of each arc can be calculated from Formula (14)–(16), where  $\mathbf{P}$  is the priori weight matrix.

$$\begin{bmatrix} \Delta\hat{h}_{l,m,l',m'} \\ \Delta\hat{V} \end{bmatrix} = (A^T P A)^{-1} A^T P \Delta\Phi \tag{14}$$

$$\Delta\hat{\Phi} = A (A^T P A)^{-1} A^T P \Delta\Phi \tag{15}$$

$$\hat{w} = \Delta\Phi - A (A^T P A)^{-1} A^T P \Delta\Phi \tag{16}$$

Equations (14)–(16) are the basic model and for the initial estimation of TCPInSAR. However, the above process assumes all arcs phase ambiguity equals to zero, which is wrong for the arcs with non-zero phase ambiguity. Therefore, L. Zhang proposed an outliers detector to find the arcs with phase ambiguity, which can be recognized by:

$$Max(|\hat{w}_i|) > c \sqrt{Max((Q^{dd})_{ii})} + 2 \sqrt{Max((Q_{\Delta\hat{\Phi}\Delta\hat{\Phi}})_{ii})} \tag{17}$$

where  $Max(\cdot)$  stands the maximum value of a vector or matrix,  $\hat{w}_i$  are the residual phases of arcs in the  $i$ th differential interferogram,  $Q^{dd}$  is the covariance matrix of the observation (differential phases at arcs), which is the inverse of matrix  $P$  in Equations (14)–(16),  $Q_{\Delta\hat{\Phi}\Delta\hat{\Phi}}$  is the covariance matrix of the observation estimation value, which can be calculated by Equation (15) and  $c$  is a constant (generally 3 or 4).

After the parameters of arcs are determined, the relationship between arcs and the points can be established by Equation (18), and we can also use the least squares method to get the parameters of each TCP.

$$\mathbf{L} = \mathbf{U} \mathbf{X} \tag{18}$$

where  $\mathbf{L}$  and  $\mathbf{X}$  are the parameters of arcs and points respectively,  $\mathbf{X} = [h_i \ V_i]$  and  $\mathbf{U}$  is the coefficient matrix that links the arcs and points, which is shown in Equation (19).  $v_i$  is the velocity of deformation of the  $i$ th interference pair.

$$\mathbf{U} = \begin{bmatrix} 1 & -1 & 0 & 0 & \cdots & 0 \\ 1 & 0 & -1 & 0 & \cdots & 0 \\ \vdots & & & & & \\ 0 & 0 & 1 & -1 & \cdots & 0 \\ \vdots & & & & & \\ 0 & 0 & 0 & \cdots & 1 & -1 \end{bmatrix} \tag{19}$$

After acquiring  $v_i$  and  $T_i$  (temporal baseline), the time-series subsidence of coherent points can be calculated using Formula (8).

### 3.4.2. Leveling Measurements

Four groups of leveling measurements, as obtained in a previous study [26], were recorded on 5 January 2012, 11 March 2012, 22 March 2012, and 2 April 2012, respectively. The four groups of leveling data are measured by the fourth level, and the error per kilometer height difference is 10 mm.

## 4. Results

### 4.1. Simulated Interferograms and Actual Interferograms

To avoid the effect of spatial decorrelation on phase unwrapping, a primary step was to simulate surface subsidence and remove it on the basis of coal mining theory. Therefore, the area with large large-scale subsidence of each image pair was simulated by the PIM and the geological mining data, and simulated subsidence was transformed into wrapped phase map. After using SRTM 3 DEM, whose resolution is 90 m, to remove the terrain phase subsets, the actual wrapped phase subsets were calculated by the SBAS technique. Residual wrapped phase subsets were obtained by subtracting simulated wrapped phase subsets from actual wrapped phase subsets generated by SBAS. The simulated wrapped phase map and actual wrapped phase map generated by SBAS are shown in Figure 4a,b, respectively. The residual wrapped phase map is shown in Figure 5.

As shown in the first five panels of Figures 4 and 5, when surface subsidence values are small, simulated subsidence values are close to values calculated by SBAS, and the numbers of stripes are significantly reduced. In the last four panels of Figures 4 and 5, simulated subsidence values are significantly different from values calculated by SBAS, and there are many stripes in residual wrapped phase map. Because wrapped phase maps simulated by PIM are regular, bulges appear in the lower right corner of interference fringes.

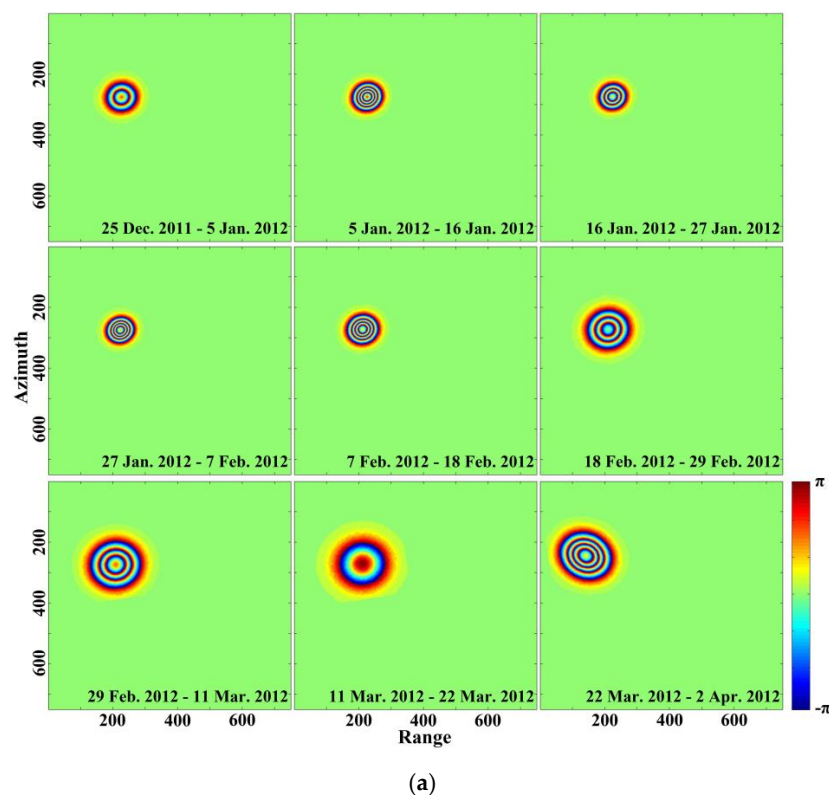


Figure 4. Cont.

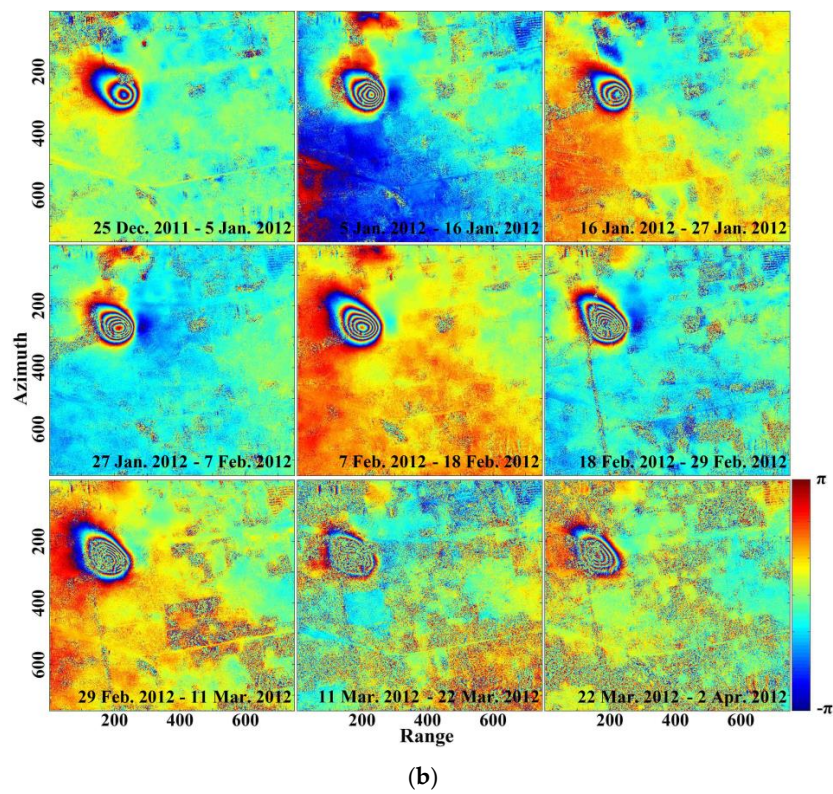


Figure 4. Simulated wrapped phase map using PIM (a) and the wrapped phase map generated by SBAS (b).

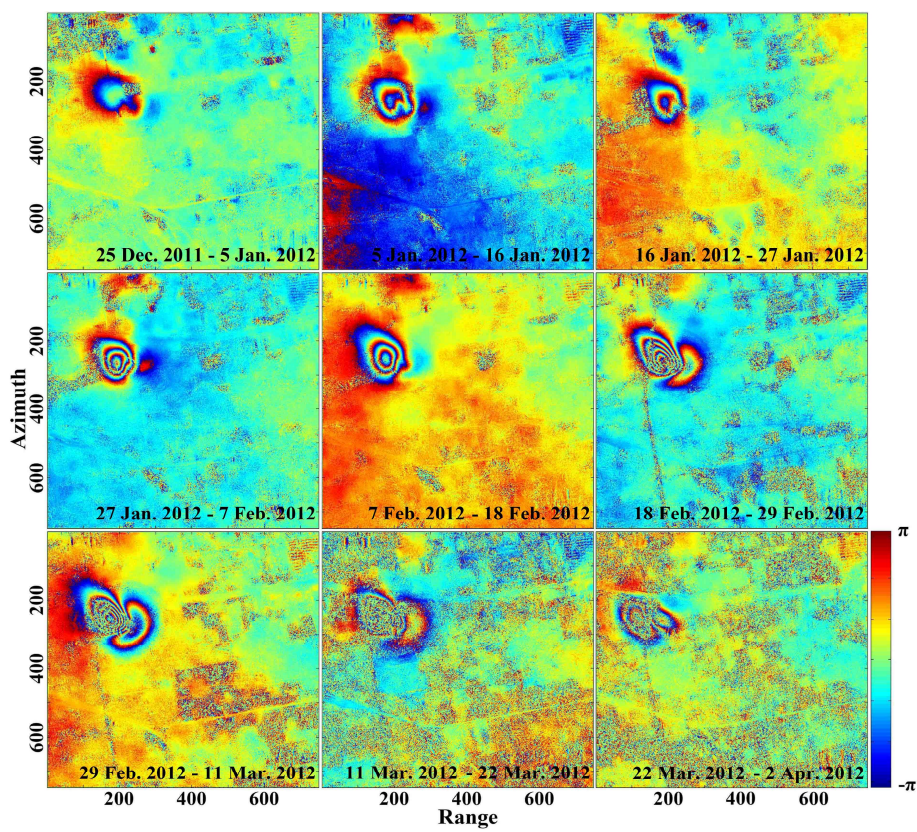


Figure 5. The residual wrapped phase map.

In addition, the subsidence of this study area was affected by the mining of 9308 workface and the residual subsidence caused by 9306 workface, an abandoned goaf near the 9308 workface. It was difficult to ensure the mining parameters of the abandoned goaf, and further, the land subsidence caused by the goaf was small; thus, we only used the 9308 workface to simulate land subsidence. The interference fringes in residual wrapped phase map are significantly reduced but not completely removed.

#### 4.2. PIM-SBAS Monitoring Results

After phase unwrapping, the coherence threshold was set to 0.2 to select the coherent points. The surface deformations were obtained by the least-squares method. Because the mining area was covered with a large number of crops in March and April, the number of coherent points in some areas was lower than in others.

A total of 152,318 coherent points were obtained. Unfortunately, few high coherence points were selected above the workface because of spatial decorrelation. Clearly, there was no evidence for land subsidence in the whole image except for the mining area. The subsidence funnel extended from the northeast to the southwest and was consistent with the mining direction. Due to the residual subsidence of the abandoned goaf (9306 workface), the range of land movements shifted to the southeast direction. The time series deformations generated by PIM-SBAS are shown in Figure 6. From 25 December 2011 to 2 April 2012, the range for the subsidence increased gradually.

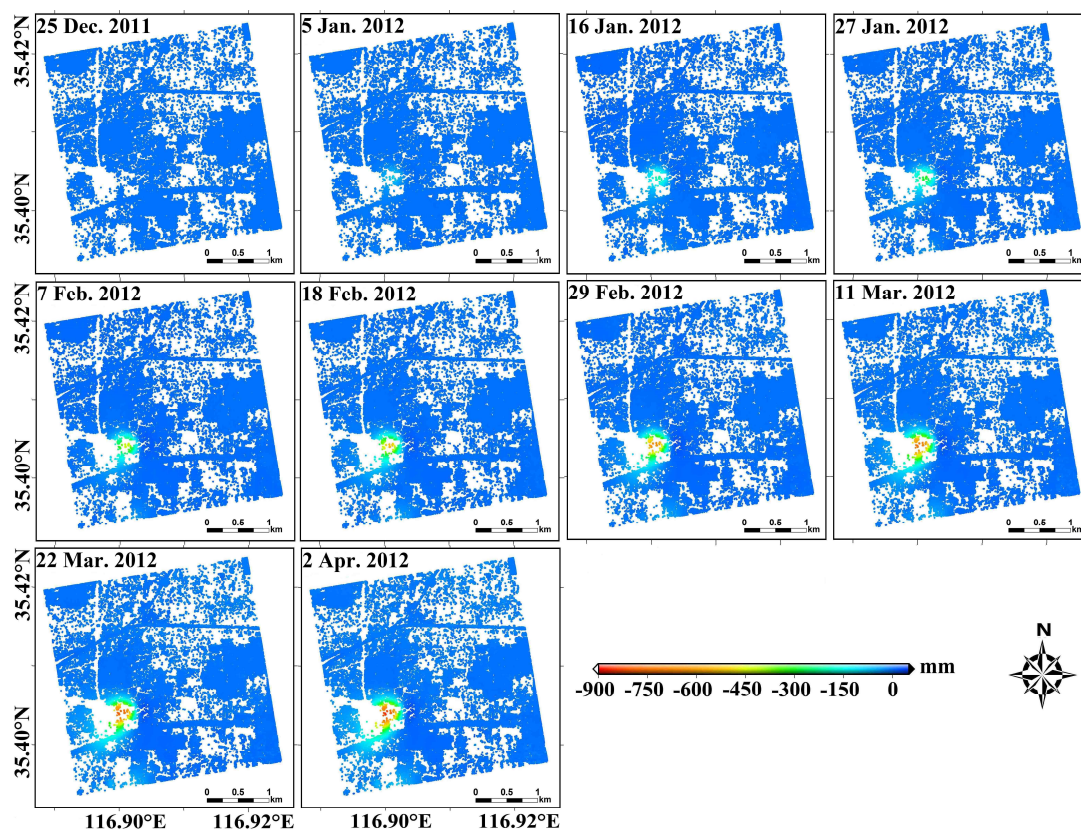


Figure 6. Time series of vertical mining subsidence generated by PIM-SBAS.

From 25 December 2011 to 2 April 2012, the maximum subsidence of coherent points reached 860 mm. Because of the spatial decorrelation caused by the large surface subsidence, the number of coherent points above the workface decreased. The number of coherent points was sufficient, however, for analysis of the influence of coal mining on the Zouji highway; the maximum subsidence of the Zouji highway was calculated to be about 145 mm.

Using PIM-SBAS, the time series subsidence values for each monitoring point were obtained; these are shown in Figure 7. As a result of the effects of mining of the 9308 workface, subsistence for almost all of the monitoring points increased over time. The monitoring point B6 attained a maximum subsidence of 142 mm on 2 April 2012.

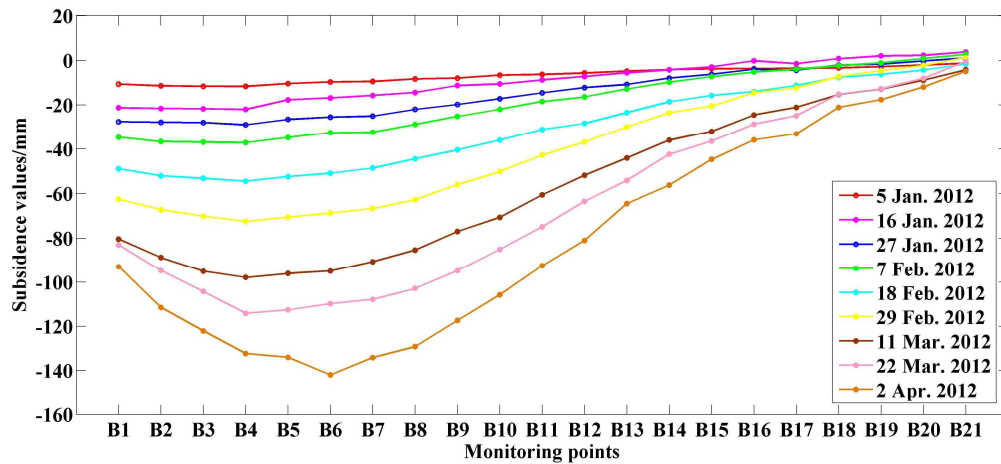


Figure 7. Accumulated subsidence of field observation points.

To effectively compare PIM-SBAS monitoring results with those obtained by other time series InSAR, the surface subsidence values obtained by SBAS and TCPInSAR were also calculated, and are presented below.

#### 4.3. Monitoring Results of SBAS and TCPInSAR

To avoid temporal and spatial decorrelation, ten TSX SAR images from 25 December 2011 to 2 April 2012, were grouped with nine interference pairs using the smallest temporal and spatial baseline. However, the surface vegetation coverage and the large surface subsidence caused spatial and temporal decorrelation, which impacted the phase unwrapping of the traditional SBAS. When the threshold of coherent values was set to 0.2, the accumulated surface subsidence from 25 December 2011 to 2 April 2012, is shown in Figure 8a.

To avoid the error introduced by phase unwrapping, TCPInSAR, a time-series InSAR for calculating surface subsidence without phase wrapping, was used to monitoring surface subsidence. After setting the coherent value to 0.2, the accumulated surface subsidence from 25 December 2011 to 2 April 2012 were mapped, and are shown in Figure 8b.

Above the 9308 workface, the maximum accumulated subsidence calculated by SBAS reached 184 mm. The maximum accumulated subsidence calculated by TCPInSAR in mining area reached 150 mm. Monitoring results of SBAS and TCPInSAR were clearly far lower than the accumulated monitoring subsidence (860 mm) calculated using PIM-SBAS.

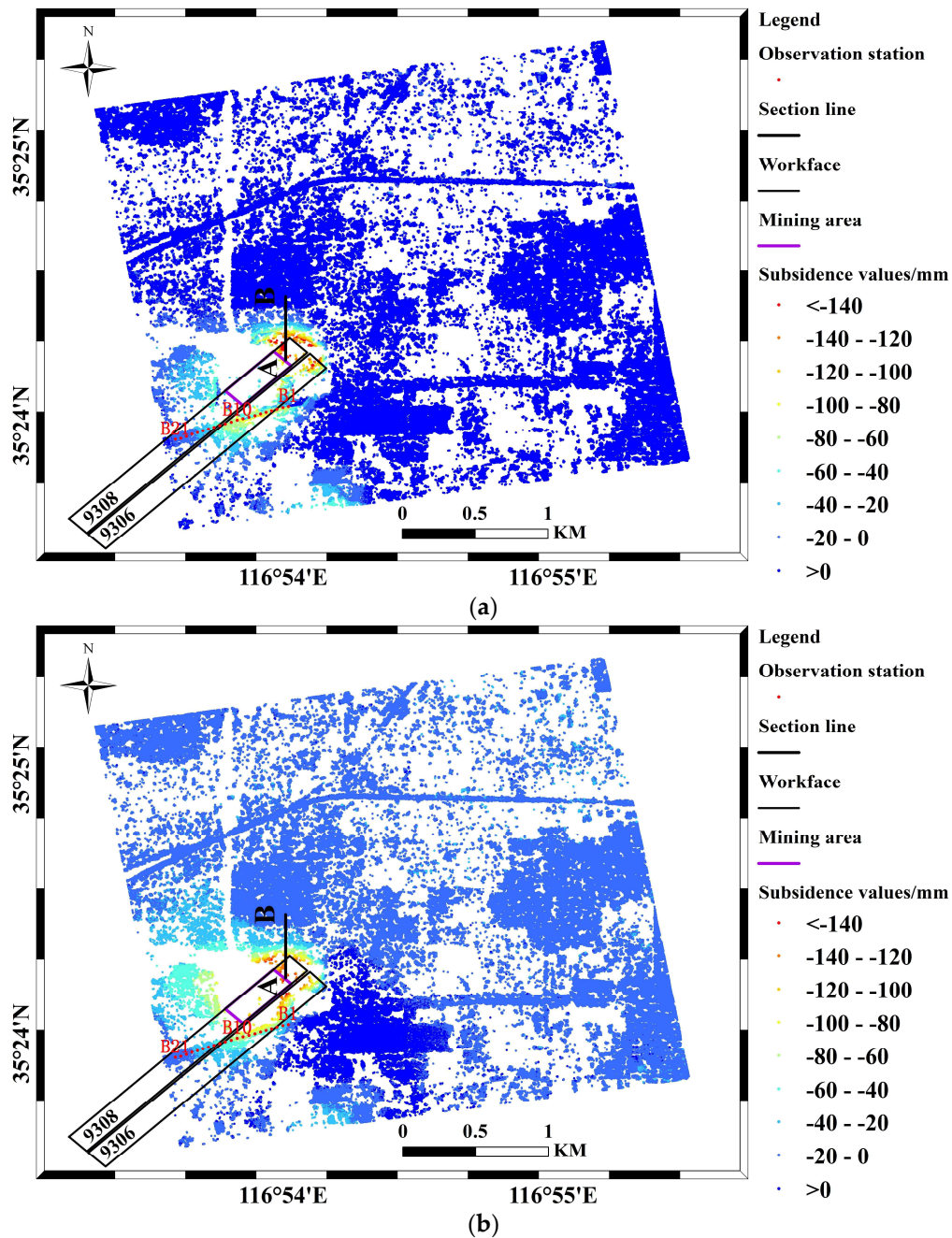


Figure 8. Accumulated surface subsidence maps generated by SBAS (a) and TCPInSAR (b).

## 5. Discussion

### 5.1. Comparison of PIM-SBAS with SBAS and TCPInSAR

In an earlier independent study, the maximum subsidence obtained was 501 mm for the period from 5 January to 11 March 2012 [30]. This value was close to the maximum subsidence calculated in our study (860 mm). It should be noted that the duration of the independent study was shorter than that of the present research. Moreover, from the ninth subpanel of Figure 4b, we can see that the land subsidence was quite extreme during the period from 11 March to 2 April 2012. This may explain why the previous subsidence value was lower than the present value. However, the results in Figure 8a,b show that subsidence values of large-scale mining subsidence generated by the TS-InSAR technique are relatively small. The main reasons for this are as follows: (1) the value of land subsidence

is large when coal is extracted, which can induce the spatial decorrelation of SAR image pairs and cause the phase unwrapping error. Even though the TCPIInSAR does not require phase unwrapping in this method, when the difference in the subsidence of the two temporarily coherent points is large, the two points are considered as existing phase ambiguities and removed. (2) Mining subsidence has a nonlinear character, while the TS-InSAR techniques (SBAS, TCPIInSAR and others) regard the main land subsidence to be linear when calculating the deformation velocity. The nonlinear deformation is calculated from the residual phase by time and the spatial filter method. The PIM-SBAS method enables resolution of these two problems. It regards the main land subsidence to be nonlinear, and this can be simulated using a mining subsidence model. The linear subsidence part is calculated by SBAS from the residual phase. Therefore, the large-scale land subsidence may be effectively generated.

### 5.2. Comparison of Results with Leveling Measurements

The Zouji highway, which passes directly above the two coal workfaces, has been seriously affected by coal extraction. To effectively monitor the subsidence of the Zouji highway due to coal mining, 21 observation stations were set up from east to west on the highway. Four groups of leveling measurements were recorded in 5 January 2012, 11 March 2012, 22 March 2012, and 2 April 2012, respectively. Two groups of leveling measurements, which were recorded in 5 January 2012, and 2 April 2012, were used to analyze the accuracy of the three methods. Subsidence values generated by the different methods during this time are shown in Figure 9.

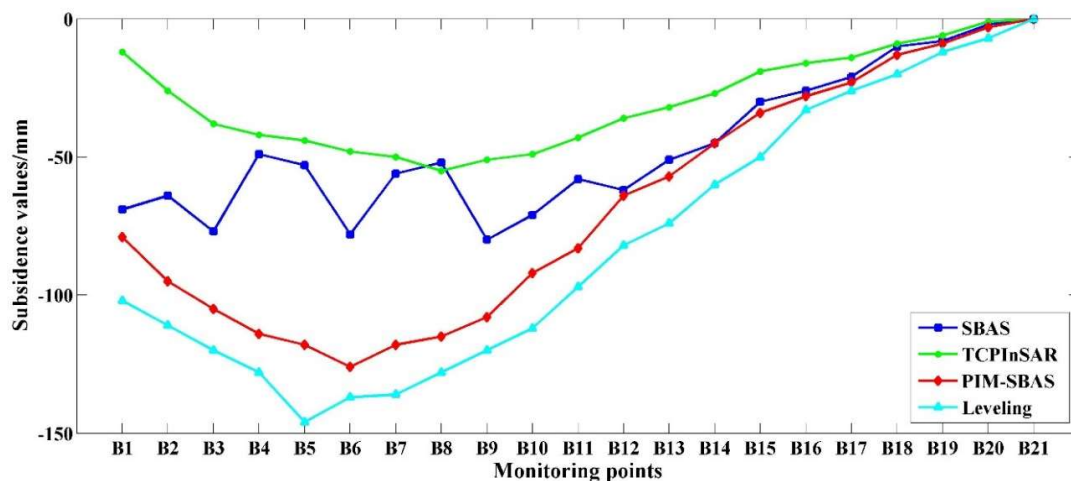


Figure 9. Subsidence values generated by different methods from 5 January to 2 April 2012.

As shown in Figure 10 and Table 2, the maximum error of the monitoring results calculated by SBAS was 93 mm, the average value was 35 mm, and the RMSE of the monitoring results was 45 mm. The maximum error of the monitoring results calculated by TCPIInSAR was 102 mm, the average value was 52 mm and the RMSE was 61 mm. The maximum error of the results calculated by PIM-SBAS was 28 mm, the average value was 13 mm, and the RMSE was 15 mm. It should be noted that these leveling points were located along the road above the abandoned goaf; therefore, the subsidence was mainly influenced by residual land deformation. Due to the simulated large-scale land subsidence not taking account of the abandoned goaf, the improved effect on these leveling points generated by PIM-SBAS was not obvious.

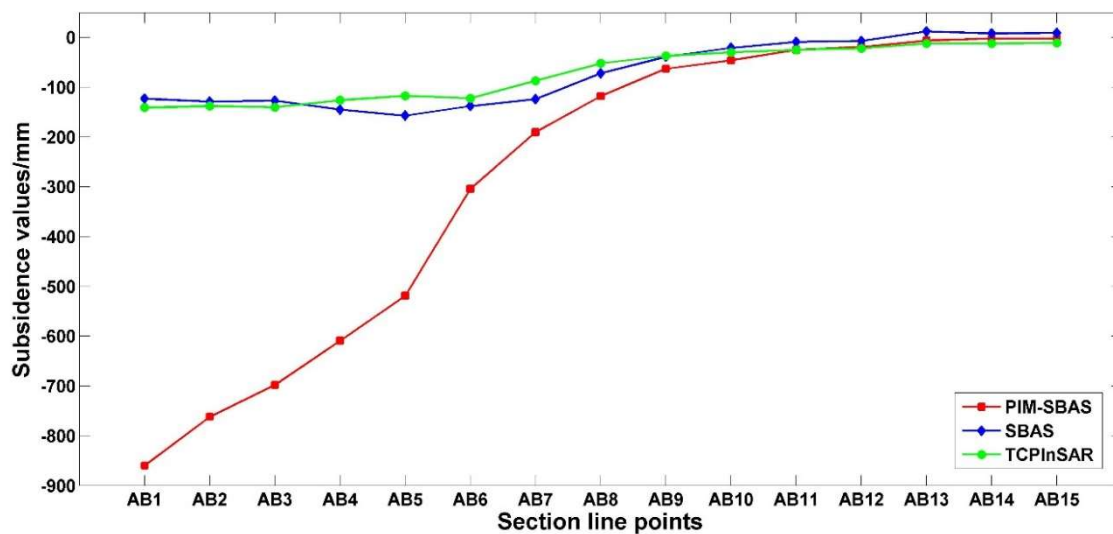


Figure 10. Accumulated subsidence for the 15 points calculated by the three TS-InSAR methods.

Table 2. Absolute errors for the three TS-InSAR methods compared with leveling observations (mm).

Surface Observation Points	SBAS	TCPInSAR	PIM-SBAS
B1	33	90	23
B2	47	85	16
B3	43	82	15
B4	79	86	14
B5	93	102	28
B6	59	89	11
B7	80	86	18
B8	76	73	13
B9	40	69	12
B10	41	63	20
B11	39	54	14
B12	20	46	18
B13	23	42	17
B14	15	33	15
B15	20	31	16
B16	7	17	5
B17	5	12	3
B18	10	11	7
B19	4	6	3
B20	5	6	4
B21	0	0	0

Although the accuracy of the PIM-SBAS monitoring results is not high, it represents an improvement over that for SBAS and TCPInSAR, especially in mining areas with large-scale subsidence. The application of PIM-InSAR for calculation of large-scale subsidence above the workplace, which is beyond the range that the traditional time series InSAR can detect, is therefore proposed. As shown in the present work, PIM-InSAR circumvents the temporal and spatial decorrelations caused by large-scale subsidence. Unfortunately, there were no field observation points above the two workfaces; therefore, we were unable to verify the effect of simulating large-scale mining subsidence using PIM-InSAR.

### 5.3. Comparison of Monitoring Results above the Workplace

The maximum subsidence values calculated by SBAS, TCPInSAR, and PIM-SBAS were 157 mm, 134 mm, and 860 mm, respectively. To confirm the different monitoring results for the three methods above the workplace, we structured a section-line that passed through the center of the subsidence

funnel. The section-line is shown in Figure 8. From A to B, a total of 15 points at 30 m intervals were selected to analyze the subsidence along the section-line. The subsidence values for the 15 points calculated by the three methods are shown in Figure 10.

As shown in Figure 10, the monitoring results of SBAS and TCPInSAR were similar to each other; however, consistent with those of PIM, the PIM-SBAS monitoring results indicated large subsidence, which closely resembled the actual situation. Thus, the PIM-SBAS method was more effective for monitoring the surface subsidence of the mining area than the other two methods.

## 6. Conclusions

A new method for subsidence monitoring, termed the PIM-SBAS method, which combines the advantages of the PIM and SBAS, was developed. This method alleviates the difficulty of phase wrapping, and enables retrieval of data for large-scale mining subsidence. Owing to the large degree of land deformation that results from coal extraction, TS-InSAR techniques (SBAS, TCPInSAR and others), which regard land subsidence as linear in order for the purpose of calculation of the deformation velocity, are not suitable for calculating mining subsidence. These TS-InSAR methods should be modified with a mining subsidence model to improve monitoring capabilities.

Time-series surface subsidence maps of Nantun coal mining area were generated using PIM-SBAS during the period from 25 December 2011 to 2 April 2012, with ten TerraSAR-X satellite images. The maximum deformation above the subsidence basin reached 860 mm. Twenty one observation stations were laid along the road from west to east, which is near the workforce. Compared with the leveling measurements, the root mean square errors of PIM-SBSA monitoring results on road and the average value of errors were 15 mm and the 13 mm respectively, which was better than the results of original SBAS and TCPInSAR methods.

As a result of the influence of substantial land deformation and vegetation, the number of coherent points above the workforce was low. To increase the number of coherent points, further studies should consider distributed scatterers and TCPs, which would enable more accurate time series monitoring of deformation above the workforce to be performed. In addition, atmospheric noises should be considered and removed using temporal filtering methods in future research. Finally, the images acquired from satellites with longer wavelengths and the offset-tracking method will be used to monitor the large-scale subsidence in mining area.

**Author Contributions:** H.F. and L.L. conceived and designed the experiments; L.L. performed the experiments; H.F., L.L. and Y.Y. contributed to data and analysis of results. L.L. wrote the paper.

**Funding:** This research was funded by the Natural Science Foundation of China (Grant No. 41604005, 41272389), the Civil Aerospace Project (No.D010102), and the Intergovernmental International Scientific and Technological Innovation Cooperation Project (Grant No. 2017YFE0107100).

**Acknowledgments:** The authors would like to thank the German Aerospace Center (DLR) for providing the TerraSAR-X images under scientific proposal LAN1173 and LAN1425.

**Conflicts of Interest:** The authors declare no conflict of interest.

## References

1. Deng, K.; Tan, Z.; Jiang, Y.; Dai, H.; Shi, Y.; Xu, L. Deformation monitoring and subsidence engineering. In *Mining Subsidence*; China University of Mining and Technology: Xuzhou, China, 2014; p. 183. (In Chinese)
2. Zhong, L.; Mann, D.; Freymueller, J.T.; Meyer, D.J. Synthetic aperture radar interferometry of Okmok volcano, Alaska: Radar observations. *J. Geophys. Res. Solid Earth* **2000**, *105*, 10791–10806.
3. Chen, Y.; Peltier, A.; Remy, D.; Perfettini, H.; Froger, J.L.; Darrozes, J.; Villeneuve, N.; Bonvalot, S. Long-term ground displacement observations using InSAR and GNSS at Piton de la Fournaise volcano between 2009 and 2014. *Remote Sens. Environ.* **2017**, *194*, 230–247. [[CrossRef](#)]
4. Ye, X.; Kaufmann, H.; Guo, X.F. Landslide monitoring in the three gorges area using D-InSAR and corner reflectors. *Photogramm. Eng. Remote Sens.* **2004**, *70*, 1167–1172. [[CrossRef](#)]

5. Massonnet, D.; Rossi, M.; Carmona, C.; Adragna, F.; Peltzer, G.; Feigl, K.; Rabaute, T. The displacement field of the Landers earthquake mapped by radar interferometry. *Nature* **1993**, *364*, 138–142. [[CrossRef](#)]
6. Ferretti, A.; Prati, C.; Rocca, F. Nonlinear subsidence rate estimation using permanent scatterers in differential SAR interferometry. *IEEE Trans. Geosci. Remote Sens.* **2000**, *38*, 2202–2212. [[CrossRef](#)]
7. Berardino, P.; Fornaro, G.; Lanari, R.; Sansosti, E. A new algorithm for surface deformation monitoring based on small baseline differential SAR interferograms. *IEEE Trans. Geosci. Remote Sens.* **2002**, *40*, 2375–2383. [[CrossRef](#)]
8. Ferretti, A.; Prati, C.; Rocca, F. Permanent scatterers in SAR interferometry. *IEEE Trans. Geosci. Remote Sens.* **2001**, *39*, 8–20. [[CrossRef](#)]
9. Kampes, B.; Hanssen, R. Ambiguity resolution for permanent scatterer interferometry. *IEEE Trans. Geosci. Remote Sens.* **2004**, *42*, 2446–2453. [[CrossRef](#)]
10. Lanari, R.; Casu, F.; Manzo, M.; Zeni, G.; Berardino, P.; Manunta, M.; Pepe, A. An overview of the small baseline subset algorithm: A dinsar technique for surface deformation analysis. *Pure Appl. Geophys.* **2007**, *164*, 637–661. [[CrossRef](#)]
11. Hooper, A.; Bekaert, D.; Spaans, K.; Arikan, M. Recent advances in SAR interferometry time series analysis for measuring crustal deformation. *Tectonophysics* **2012**, *514*, 1–13. [[CrossRef](#)]
12. Hooper, A. A multi-temporal InSAR method incorporating both persistent scatterer and small baseline approaches. *Geophys. Res. Lett.* **2008**, *35*. [[CrossRef](#)]
13. Zhang, L.; Ding, X.; Lu, Z. Modeling PSInSAR time series without phase unwrapping. *IEEE Trans. Geosci. Remote Sens.* **2011**, *49*, 547–557. [[CrossRef](#)]
14. Zhang, L.; Ding, X.; Lu, Z. Ground settlement monitoring based on temporarily coherent points between two SAR acquisitions. *ISPRS J. Photogramm. Remote Sens.* **2011**, *66*, 146–152. [[CrossRef](#)]
15. Werner, C.; Wegmüller, U.; Strozzi, T.; Wiesmann, A. Interferometric point target analysis for deformation mapping. In Proceedings of the 2003 IEEE International Geoscience and Remote Sensing Symposium, IGARSS '03, Toulouse, France, 21–25 July 2003; pp. 4362–4364. [[CrossRef](#)]
16. Blanco-Sánchez, P.; Mallorquí, J.; Duque, S.; Monells, D. The Coherent Pixels Technique (CPT): An Advanced DInSAR Technique for Nonlinear Deformation Monitoring. *Pure Appl. Geophys.* **2008**, *165*, 1167–1193. [[CrossRef](#)]
17. Rocca, F. Modeling interferogram stacks. *IEEE Trans. Geosci. Remote Sens.* **2007**, *45*, 3289–3299. [[CrossRef](#)]
18. Ferretti, A.; Fumagalli, A.; Novali, F.; Prati, C.; Rocca, F.; Rucci, A. A new algorithm for processing interferometric data-stacks: SqueeSAR. *IEEE Trans. Geosci. Remote Sens.* **2011**, *49*, 3460–3470. [[CrossRef](#)]
19. Fornaro, G.; Verde, S.; Reale, D.; Pauciuolo, A. CAESAR: An approach based on covariance matrix decomposition to improve multibaseline-multitemporal interferometric SAR processing. *IEEE Trans. Geosci. Remote Sens.* **2015**, *53*, 2050–2065. [[CrossRef](#)]
20. Cao, N.; Lee, H.; Jung, H. A Phase-Decomposition-Based PSInSAR Processing Method. *IEEE Trans. Geosci. Remote Sens.* **2016**, *54*, 1074–1090. [[CrossRef](#)]
21. Samsonov, S.; D'Oreye, N.; Smets, B. Ground deformation associated with post-mining activity at the French–German border revealed by novel InSAR time series method. *Int. J. Appl. Earth Obs. Geoinf.* **2013**, *23*, 142–154. [[CrossRef](#)]
22. Wegmüller, U.; Walter, D.; Spreckels, V.; Werner, C. Nonuniform ground motion monitoring with TerraSAR-X persistent scatterer interferometry. *IEEE Trans. Geosci. Remote Sens.* **2010**, *48*, 895–904. [[CrossRef](#)]
23. Cuenca, M.; Hooper, A.; Hanssen, R. Surface deformation induced by water influx in the abandoned coal mines in Limburg, the Netherlands observed by satellite radar interferometry. *J. Appl. Remote Sens.* **2013**, *88*, 1–11. [[CrossRef](#)]
24. Bateson, L.; Cigna, F.; Boon, D.; Sowter, A. The application of the Intermittent SBAS (ISBAS) InSAR method to the South Wales Coalfield, UK. *Int. J. Appl. Earth Obs. Geoinf.* **2015**, *34*, 249–257. [[CrossRef](#)]
25. Fan, H.; Gu, W.; Qin, Y.; Xue, J.; Chen, B. A model for extracting large deformation mining subsidence using D-InSAR technique and probability integral method. *Trans. Nonferrous Met. Soc. China* **2014**, *24*, 1242–1247. [[CrossRef](#)]
26. Zhao, B.; Li, H.; Guo, G.; Mi, L. Study on high-precision regional monitoring method of high-grade highways subsidence under the influence of underground mining. *Surv. Rev.* **2016**, *4*, 1–12. [[CrossRef](#)]

27. Fan, H.; Xu, Q.; Hu, Z.; Du, S. Using temporarily coherent point interferometric synthetic aperture radar for land subsidence monitoring in a mining region of western China. *J. Appl. Remote Sens.* **2017**, *11*, 026003. [[CrossRef](#)]
28. Diao, X.; Wu, K.; Zhou, D.; Li, L. Integrating the probability integral method for subsidence prediction and differential synthetic aperture radar interferometry for monitoring mining subsidence in Fengfeng, China. *J. Appl. Remote Sens.* **2016**, *10*, 016028. [[CrossRef](#)]
29. He, G.; Yang, L.; Ling, G. General regulations of land movement and deformation during coal exploitation. In *Mining Subsidence*; China University of Mining and Technology: Xuzhou, China, 1991; pp. 85–86. (In Chinese)
30. Zhang, W.; Guo, G.; Guo, Q. Surface subsidence monitoring in mining area based on D-InSAR. *Coal Eng.* **2017**, *49*, 122–124. (In Chinese) [[CrossRef](#)]



© 2018 by the authors. Licensee MDPI, Basel, Switzerland. This article is an open access article distributed under the terms and conditions of the Creative Commons Attribution (CC BY) license (<http://creativecommons.org/licenses/by/4.0/>).